PCCP

PAPER

View Article Online
View Journal | View Issue

Cite this: *Phys. Chem. Chem. Phys.*, 2017, **19**, 20029

Lithiation of multilayer Ni/NiO electrodes: criticality of nickel layer thicknesses on conversion reaction kinetics†

Guennadi Evmenenko,[a] Timothy T. Fister,[b] D. Bruce Buchholz,[a] Fernando C. Castro,[c] Qianqian Li,[c] Jinsong Wu,[ac] Vinayak P. Dravid,[a] Paul Fenter *[b] and Michael J. Bedzyk *[ad]

Received 15th April 2017,
Accepted 11th July 2017

DOI: 10.1039/c7cp02448g

rsc.li/pccp

X-ray reflectivity and transmission electron microscopy (TEM) were used to characterize the morphological changes in thin film electrodes with alternating Ni and NiO layers during lithiation as a function of the Ni buffer layer thickness. Complete lithiation of the active NiO layers occurs only when the thickness of the Ni/NiO bilayers are less than 75 Å – a threshold value that is determined by the sum of the Ni quantity in the Ni/NiO bilayer of the multilayer stack. Thicker Ni/NiO bilayers present a kinetic barrier for lithium ion diffusion inside the stack resulting in partial lithiation of the multilayer electrodes in which only the top NiO layer lithiates. Lithiation of NiO layers in a multilayer stack also leads to an interface-specific reaction that is observed to increase the thicknesses of adjacent Ni layers by 3–4 Å and is associated with the formation of a low-density Li_2O layer, corresponding to an interfacially-driven phase separation of the NiO. Rate dependent cyclic voltammetry studies reveal a linear relation between the peak current and scan rate suggesting that the lithiation kinetics are controlled by charge transfer resistance at the liquid–solid interface.

Introduction

The performance of lithium-ion battery (LIB) electrodes is largely governed by the starting morphology and chemical composition, and evolution during electrochemical reactions. Much like conductive binders in bulk electrodes, an effective way to improve the electrochemical performance of thin film LIB electrodes is to introduce a secondary material that can facilitate electronic or lithium transport. This layer can also be used to alleviate the volume change in the electrode and to prevent the aggregation of active materials. For lithium ion anode materials, an effective implementation of this concept is to use a multilayer thin film structure comprised of ~nm-thick Si (or other high capacity materials) and inert metal layers (*e.g.*, Ti, Al, Zn). Recent studies of Si-based multilayer electrodes show strong increases in reversible capacity and cycling stability as a function of the thicknesses of the buffer and active layers.[1–12] For example, in the case of Si/Fe multilayers, it has been found that thin Fe buffer layers (<200 Å) can lead to a higher capacity of Si/Fe multilayer film, which is related to the fast transport of the Li ions, but cyclic performance deteriorates with repeated cycling.[5] In contrast, thicker Fe layers (800 Å) and increasing the number of bilayer stacks (from 5 up to 16) improves the cycle life with high reversibility. In our previous work, we demonstrated that multilayers consisting of alternating amorphous silicon thin films and planar, conducting "adhesive layers" of Cr_xSi ($x \approx 3$) combine the intrinsically high Li-capacity of silicon, the reversibility of ultrathin silicon films, and the conductivity of a composite material.[7] The multilayer electrodes also show enhanced long-term cyclability and rate capabilities relative to a comparable silicon thin film electrode.

Here, we are interested in understanding approaches for controlling the lithiation reactions of metal-oxides. NiO, a prototypical Li-ion conversion material is a conceptually promising electrode material for LIBs due to abundance, low cost, and high theoretical specific capacity (718 mA h g^{-1}). First demonstrated by Tarascon *et al.*,[13] the lithiation of NiO follows a displacement process with the reversible formation of Li_2O accompanied by the reduction of the transition metal leading to aggregated Ni nanoparticles in the range of 10–100 Å in diameter: $NiO + 2Li^+ + 2e^- \leftrightarrow Ni + Li_2O$. However, the implementation of NiO and other conversion electrodes in LIBs is greatly hindered

[a] *Department of Materials Science and Engineering, Northwestern University, Evanston, Illinois 60208, USA. E-mail: bedzyk@northwestern.edu*
[b] *Chemical Sciences and Engineering Division, Argonne National Laboratory, Lemont, Illinois 60439, USA*
[c] *EPIC, NUANCE Center, Northwestern University, Evanston, Illinois 60208, USA*
[d] *Department of Physics and Astronomy, Northwestern University, Evanston, Illinois 60208, USA*

† Electronic supplementary information (ESI) available. See DOI: 10.1039/c7cp02448g

by a number of factors, including its poor long-term cycling stability and rate performance due to the significant dimensional and volumetric changes during electrochemical cycling deformations and degradation of the electrode, including fragmentation, disintegration, fracturing, and loss in contact between current collectors and the active electrode materials.[14] A second significant issue is the substantial overpotentials[15] that are generally observed with conversion materials, which has been that are associated with the nucleation of metal nanoparticles within a Li_2O matrix.

Recent studies of the structural evolution of multi-bilayer Ni/NiO films with active NiO layers sandwiched between buffer Ni layers led a new understanding of lithiation mechanism in these model Li-ion battery (LIB) electrodes.[16] We demonstrated that the confinement of nanometer-scale NiO layers within a Ni/NiO multilayer electrode can direct lithium transport and reactivity, leading to coherent expansion of the multilayer. In particular, the nm-thick nickel layers helps to initiate the conversion process at the interface and then provides an architecture that confines the lithiation to the individual oxide layers. XRR data revealed that the lithiation process starts at the top and progressed through the electrode stack, resulting in layer by layer lithiation with a purely vertical expansion. Our observations provided new insights into the role of metal/metal oxide interfaces in controlling lithium ion conversion reactions by defining the relationships between morphological changes and film architecture during reaction. The ultrathin morphology is critical for achieving fast and durable Li^+ storage that was shown recently for Ni/NiO hybrid nanomembranes[17] and NiO nanosheets.[18]

The aim of the present study is to better understand the thickness of the individual layers in the multilayer framework affects this 1D confinement and the kinetics of lithiation. Just as in bulk batteries, where the mobility of charge carriers is central to observed charging rates and overpotentials, lithium ion transport plays a critical role for multilayer film electrodes. Generally, it is assumed that the rate-determining step for lithiation of an electrode is controlled by Li diffusion inside the active material.[19] While lithium transport within the active material is often rate-limiting in bulk intermetallic materials,[20] the abrupt metal interfaces within a multilayer architecture (in this case, Ni) may hinder Li transport through the overall stack, and we expect this barrier to be potential- and thickness-dependent. This type of planar interface is useful for characterizing transport phenomenena at the metal/oxide interface as well as understanding barriers for transport in a conversion reaction. Such a model system is necessary to better understand the complex network of interfaces that forms between the nanoscale products of a conversion reaction.

Since lithiation of a conversion material occurs through dramatic structural and morphological modifications of an electrode, we apply *in operando* and *ex situ* X-ray scattering techniques, and cross-sectional transmission electron microscopy (TEM) for systematic studies of multilayer Ni/NiO films with varying thicknesses of active and buffer layers (10 Å to 200 Å) and numbers of periodic bilayers (2 and 5). Herein, we analyze Ni/NiO multilayer electrodes to address how the electrode lithiation characteristics are affected by two key architectural parameters: (1) the thickness of the Ni layers and (2) the choice of the layer (Ni *vs.* NiO) at the electrode/electrolyte interface. Two different sets of films were deposited by PLD: Ni/NiO/Ni trilayers with varied thicknesses of top Ni layer and 2-bilayer Ni/NiO films with different thicknesses of Ni layer in the top bilayer. We show criticality of nickel layer thicknesses on conversion reaction kinetics of the active NiO layers. Thick Ni/NiO bilayers present a kinetic barrier for lithium ion diffusion inside the stack resulting in partial lithiation of the multilayer electrodes in which only the top NiO layer lithiates. Complete lithiation of NiO layers occurs only when the thickness of the Ni/NiO bilayers are less than the characteristic threshold value. We found that this conversion reaction is not diffusion limited at the level of the few nm-thick films.

Experimental

The nickel metal/nickel oxide multilayer films were grown by pulsed-laser deposition (PLD) on 10 × 3 × 1 mm sapphire α-Al_2O_3 (1–102) substrates (CrysTec GmbH, Germany). Each sample was fully immersed in a 'transmission-geometry' X-ray compatible electrochemical cell[21] such that the scattering plane aligned along the shorter 3 mm dimension. Separate Ni and NiO PLD targets were used to grow the multilayer films with thicknesses of each layer controlled by adjusting the number of laser pulses. Each heterostructure was masked from the bottom nickel layer, providing 3 mm tabs for electrical contact from top spring electrodes.

The *in operando* X-ray reflectivity (XRR) experiments were performed at sector 33BM at the Advanced Photon Source (APS) at photon energies of E = 20.00 keV and 17.50 keV.[22] The X-ray beam was collimated to 1.0 × 0.25 mm^2 and the scattered X-ray intensity was acquired with a Pilatus 100k detector. Full reflectivity data scans were measured in 15 min and were collected repeatedly during electrochemical cycling. The electrochemical cell had separate lithium metal counter and reference electrodes[21] and was fully immersed in a 1 M solution of $LiPF_6$ or $LiClO_4$ in a 1 : 1 ratio of ethylene carbonate and dimethyl carbonate by volume. The choice of salt is known to affect the composition and thickness of solid electrolyte interphase, but was found to not alter structural changes during lithiation at the studied potentials ($\sim$0.6 V). A CHI760E electrochemical workstation was used for electrochemical control of lithiation. *Ex situ* XRR studies of lithiated samples after first discharge cycle were carried out at a Rigaku ATXG diffractometer (NU X-ray Diffraction Facility) with E = 8.04 keV (λ = 1.54 Å) X-rays collimated to 0.1 × 2.0 mm^2 spot. All XRR measurements were performed at ambient laboratory temperature, which ranged between 20 to 25 °C.

XRR analysis used Motofit[23] with a multiple-slab model that included a sapphire substrate, 1–5 Ni/NiO bilayers, and an electrolyte (*in operando*) or air (*ex situ* experiments). Structural parameters for sapphire and the electrolyte were fixed, whereas the parameters for the buffer and active layers (electron density, interface roughness, and layer thickness) were allowed to vary.

The electron densities were initially estimated based on the chemical composition of the multilayer electrode components. Table S1 (ESI†) lists calculated electron densities of bulk materials relevant to this study. For lithiated samples the structural model included variable electron densities and thicknesses of active NiO-based layers and variable Ni-layer thicknesses with an electron density that was fixed to a value obtained from the analysis of the pristine as-deposited samples. In some cases, the fits made use of a parameter that nominally varies the energy resolution of the X-ray beam. In this case, this parameter is used as a phenomenological approach to incorporate the lateral heterogeneity of the multilayer structure (*e.g.*, the layer spacing).

The cross section samples of the lithiated and partially lithiated thin films were prepared using a focused ion beam (FIB) system (FEI Helios Nanolab 600 DualBeam FIB/SEM). First, bulk FIB milling techniques were used to isolate the cross-section area of interest. The lamellae were then mounted onto an Omniprobe® Lift-Out TEM Grid and further thinned with low energy gallium ions to obtain electron transparent samples with minimal FIB-induced damage. Scanning transmission electron microscopy (STEM) imaging and electron energy loss spectroscopy (EELS) analysis were carried out on the lamellae using a JEOL 2100F TEM/STEM operating at 200 kV (0.02508 Å electron wavelength) and equipped with a Gatan GIF system capable of operating with a 1 eV EELS energy resolution, as measured by the FWHM of the zero-loss peak.

Results and discussion

In operando XRR measurements of structural changes in multilayer Ni/NiO electrode during the first discharge (*i.e.* lithiation) of a half-cell consisting of the film and a lithium metal reference electrode were performed under potentiostatic control starting at the open circuit condition (3.0–3.3 V). In our recently reported work, we show that the lithiation process of the vertically digitized multilayer Ni/NiO electrodes with 20 Å-thick Ni layers and varied thicknesses of NiO layers starts at the top NiO layer and then progresses towards the bottom of the stack.[16] The overall thickness of the lithiated multilayer film increased to approximately twice the original thickness accompanied by a lowering of the electron density of the active layers from 2.04 e^{-} $Å^{-3}$ to 1.1 e^{-} $Å^{-3}$ corresponding to a confined layer of Ni nanoparticles within a Li_2O matrix. This is close to the expected density of 1.20 e^{-} $Å^{-3}$, which corresponds to the stoichiometric composition of Ni and Li_2O after NiO is fully lithiated as a result of the conversion reaction. The XRR data analysis indicates a uniform electron density profile within each oxide layer, implying that the reduced Ni nanoparticles are randomly distributed within the Li_2O matrix without locally expressed variations within each layer and between different layers of the multilayer structure. This 'confinement' effect provides much needed structural stability during conversion, but could ultimately limit lithium diffusion through the heterostructure. Experiments in this study were performed on a range of Ni/NiO heterostructures with varying layer thickness to better understand the role of Ni barrier layers on the electrochemical activity of the overall electrode structure.

NiO terminated 5-bilayer Ni/NiO electrodes

As a first example, we examine the effect of increasing the metal layer thickness from our previous study from 20 Å to 55 Å.[16] In operando X-ray reflectivity patterns were measured repeatedly during multiple cyclic voltammetry (CV) scans between the open circuit potential of the pristine structure and 0.3 V (with respect to Li/Li^{+}) with the sweep rate of 0.2 mV s^{-1} for 5-bilayer Ni/NiO film with 55 Å and 50 Å-thick Ni and NiO layers, respectively. The first cycle voltammogram taken during these measurements is shown in Fig. 1. This voltammogram has the expected reductive and oxidative features, which are characteristic for lithiation behavior of NiO electrodes.[24–26] An abrupt onset of lithiation occurs near 0.70 V during the first cathodic scan corresponding to the reduction of NiO to metallic Ni.

The amount of inserted lithium was estimated from the first cycle voltammogram and shows that the lithiated film reaches about 25% of its theoretical capacity of ~1.4 mA h for a fully lithiated NiO multilayer electrode. Such partial lithiation of the Ni/NiO multilayer film was confirmed by XRR and TEM. Fig. 2A shows specular X-ray reflectivity patterns for the pristine and the lithiated films in the first three lithiation cycles. The XRR patterns show no systematic shift of multilayer Bragg peaks during lithiation, as was previously observed for fully lithiated Ni/NiO multilayer films.[16] However, XRR data do indicate some changes between Bragg peaks. The corresponding electron density profiles derived from best fits are shown in Fig. 2B, where one can see that only the top layer of NiO was lithiated, effectively doubling of its thickness with a ~twofold decrease of its electron density, as is characteristic for a fully lithiated NiO film. Since the four other NiO layers of the 5-bilayer Ni/NiO film are unchanged during the first 3 cycles, the results reveal that the top Ni layer in the stack acts as a barrier for lithium ion transport through the overall multilayer film.

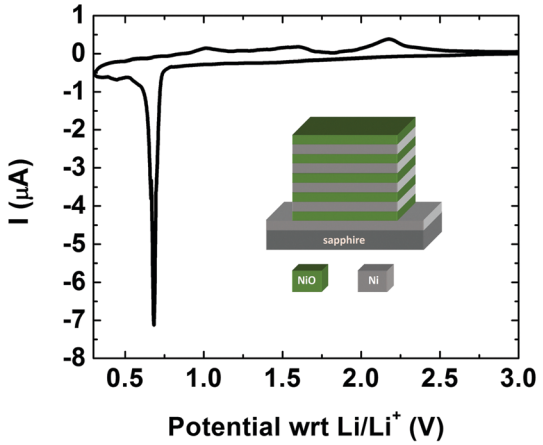

Fig. 1 The first cycle voltammogram of a 5-bilayer Ni/NiO (55 Å/50 Å) structure. Schematic illustration of pristine 5-bilayer film is shown in the inset.

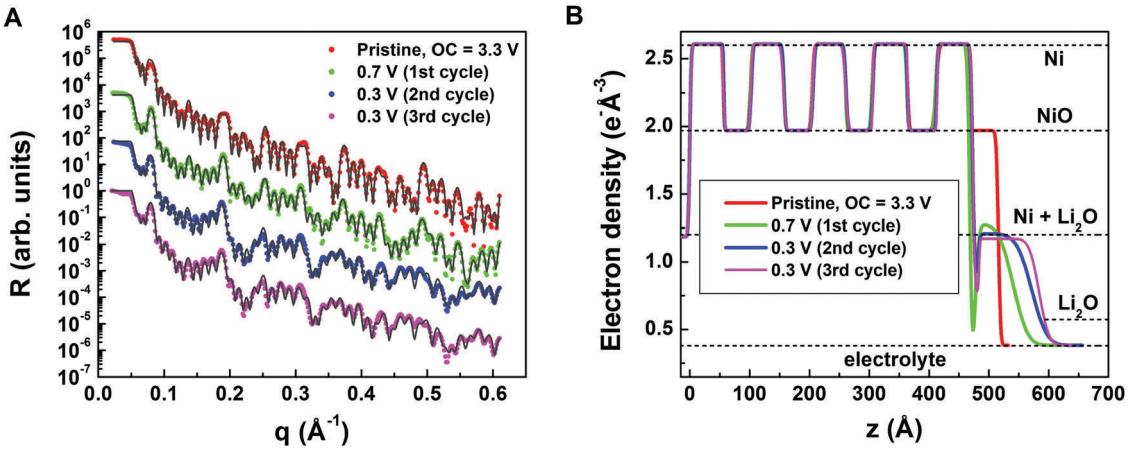

Fig. 2 (A) The specular XRR data (solid circles) and best fits (solid lines) for the pristine and lithiated 5-bilayer Ni/NiO (55 Å/50 Å) structures. Each set of experimental and model-fit curves are shifted vertically for clarity. (B) Electron density profiles obtained from best fits of the XRR data shown in A. Calculated electron densities for the electrolyte, Ni, NiO, Li_2O and expected electron density of the fully lithiated NiO layer (Ni + Li_2O) are shown by dotted lines for comparison.

XRR analysis also reveals the presence of a lower-density 10 Å region that is formed adjacent to the underlying Ni surface. We assume that such decreasing of electron density is due to nucleation of the conversion reaction at the nickel interface, leading to a an increased concentration of Li_2O at this interface. Consistent with the presence of a Li_2O layer, the XRR-derived electron density profiles (Fig. 2B) also shows that top Ni layer increases in thickness by ~4 Å following lithiation, indicating that the underlying metal layer plays a role in the conversion reaction at its interface. Such Ni nucleation at the Ni-NiO interfaces was found in our previous study,[16] where an increased thickness of each buffer Ni layer by 6–7 Å was observed for the lithiated sample due to growth of reduced Ni on both sides of the original Ni layers. Slight structural changes of the top lithiated NiO layer is observed during 2nd and 3rd cycles.

After sweeping potential to 0.3 V in the 3rd cycle, the lithiated sample was imaged by *ex situ* cross-sectional TEM. Fig. 3 confirms our XRR results; showing that only the top layer of the Ni/NiO multilayer film was lithiated. This image also reveals a low-density region between the top Ni layer and the lithiated Ni/Li_2O layer, consistent with the low density region observed by XRR. This conclusion was further supported by the nano-beam electron diffraction (Fig. 4). The diffraction patterns show both Ni and NiO diffraction rings in the non-reacted region of the multilayer film without any evidence of Li_2O. Whereas in the reacted region, very clear Ni diffraction rings and very weak rings of Li_2O crystal are observed, but there are no rings that can be indexed as NiO. Electron energy-loss spectroscopy mapping of the reacted region shows clear signals of Li, Ni and O (Fig. S1, ESI†). Hence, these results reveal the importance of the buffer layer thickness for lithium ion permeability through overall multilayer structure for lithiation of all active layers.

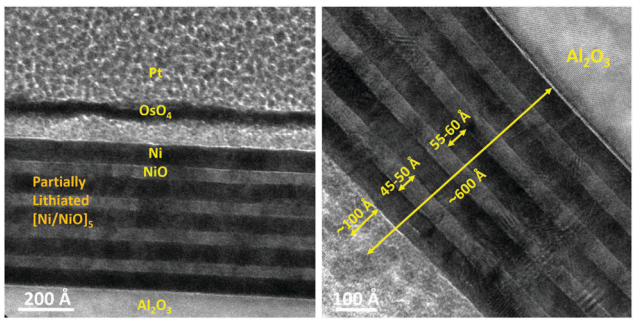

Fig. 3 The cross-sectional TEM image of the partially lithiated 5-bilayer Ni/NiO (55 Å/50 Å) film (the darker contrast represents heavier elements).

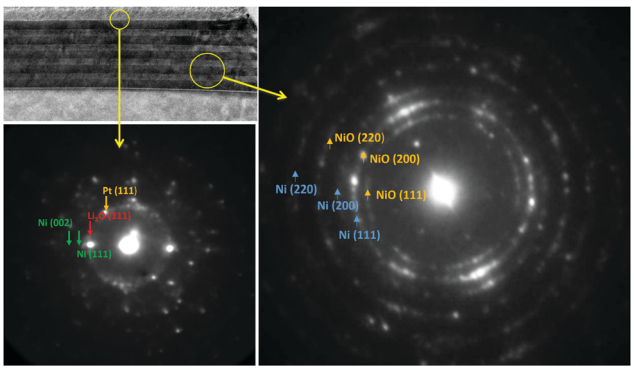

Fig. 4 Nano-beam electron diffraction patterns of the partially lithiated 5-bilayer Ni/NiO (55 Å/50 Å) film for (bottom left) the outermost NiO layer showing complete transformation to Li_2O and (right) within the deeper Ni/NiO layers showing no evidence of conversion of the NiO layer.

Ni terminated Ni/NiO/Ni trilayer structures

To clarify the question concerning the role of buffer layers in multilayer electrodes, we deposited two different sets of Ni/NiO/Ni trilayer structures having the same NiO/Ni bilayer structure with different thicknesses for the Ni capping layer to explore how variations of the top Ni layers influences lithiation kinetics within the multilayer film. Fig. 5 shows the first discharge

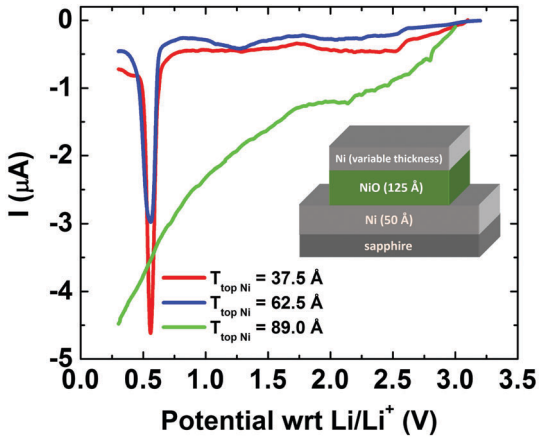

Fig. 5 The first discharge voltammograms for trilayer Ni/NiO/Ni electrodes with top Ni layer of varied thickness. Schematic illustration of pristine trilayer film is shown in the inset.

scans between the open circuit potential and 0.3 V with the sweep rate of 0.1 mV s^{-1} for the trilayer Ni/NiO/Ni films with 50 Å (Ni), 125 Å (NiO) and varied thickness of the top Ni layer. When the thickness of the top Ni layer is 37.5 Å or 62.5 Å, the scan shows a typical profile, with a clear cathodic wave characteristic for NiO lithiation. The abrupt onset of lithiation occurs near 0.56 V which is slightly lower than the 0.70 V onset observed for the NiO-terminated structure shown in Fig. 1. The integrated charge of these lithiated films is close to theoretical capacity of ~0.7 mA h assuming complete lithiation of the NiO layer. In contrast, a featureless cathodic wave was obtained for the trilayer film with a top 89 Å thick Ni layer. After the first discharge scans were completed (at 0.3 V), the samples were removed from electrochemical cells and rinsed with dimethyl carbonate (DMC).[27] X-ray reflectivity measurements were used to determine the structural changes in these samples.

Fig. 6 shows the *ex situ* specular reflectivity data and associated density profiles for the lithiated trilayer films with 37.5 Å and 62.5 Å-thick top layer Ni layers. Fits to the XRR data confirm that the NiO layer was lithiated with the expected changes in thickness and electron density for both films. Electron density profiles (Fig. 6B) indicate the creation of narrow (10–15 Å) low density regions near one of the Ni/NiO interfaces, where the electron density dips below that of the lithiation Ni/L_2O layers, and has a value consistent with that of pure Li_2O. This can be explained by a non-uniformity in the conversion reaction at these interfaces, similar to the reaction discussed above. While the behavior of the structure with the top 62.5 A-thick Ni layer was generally ideal with only little change in the Ni layers, the XRR data analysis shows that lithiation of the structure with $T_{top\text{-}Ni}$ = 37.5 Å film caused a significant reduction in density for the top Ni layer and an increased density for the lithiated NiO interlayer. This can be explained by a lateral non-uniformity in expansion of the active layer during lithium ion insertion, which could introduce porosity to the top nickel layer. It was recently reported that phase conversion of NiO can nucleate from spatially distant locations on the same slab of material.[28] Electron density profiles in Fig. 6B show that lithium ions penetrate through the top Ni layer and that the NiO interlayer undergoes a conversion reaction even when the top Ni layer has a 62.5 Å thickness. However, if thickness of the top Ni layer increases to 89 Å, the electron density profiles for the pristine trilayer film and the same film after the first discharge cycle are similar (Fig. S2, ESI†) with no lithiation of the intermediate NiO layer. This reveals that there is an effective threshold for lithium passage through the top Ni capping layer in trilayer Ni/NiO/Ni films within the thickness range of 63–89 Å.

NiO terminated 2-bilayer Ni/NiO electrodes

The apparent lithiation potentials of 5-bilayer and trilayer NiO-based electrodes was found to be 0.70 V and 0.56 V, respectively (Fig. 1 and 5). We expect that this difference in lithiation potential is controlled by the termination of the electrode stack with a Ni or NiO top layer. To check this assumption, we deposited 2-bilayer Ni/NiO structures with NiO layers of 60 Å thick, a bottom Ni layer thickness of 52 Å thick, and with a variable thickness of the top Ni layer: 16 Å, 37 Å, 58 Å and 82 Å (see XRR data and

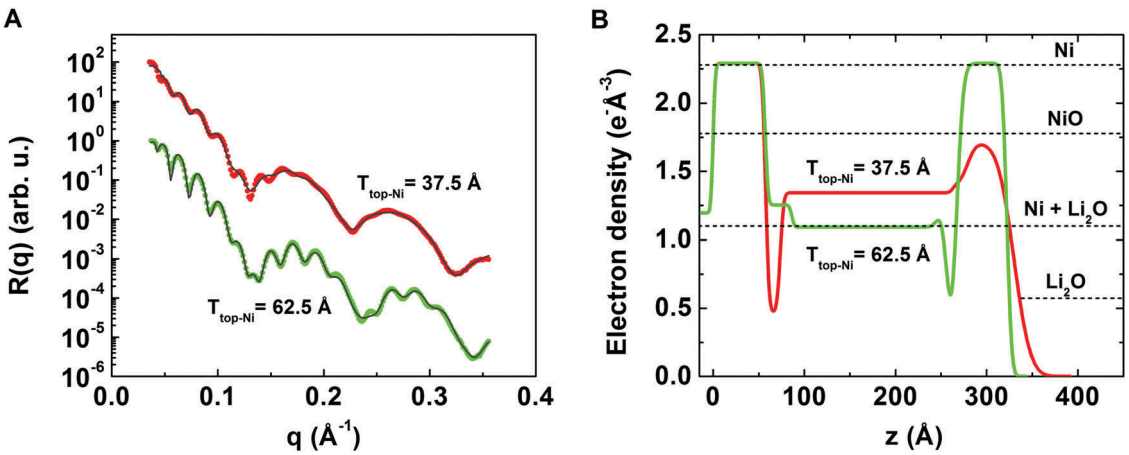

Fig. 6 (A) The specular XRR data (solid circles) and best fits (solid lines) for lithiated trilayer Ni/NiO/Ni films. The experimental and theoretical curves are shifted vertically for clarity. (B) Electron density profiles obtained from best fits of the XRR data shown in Fig. 6A.

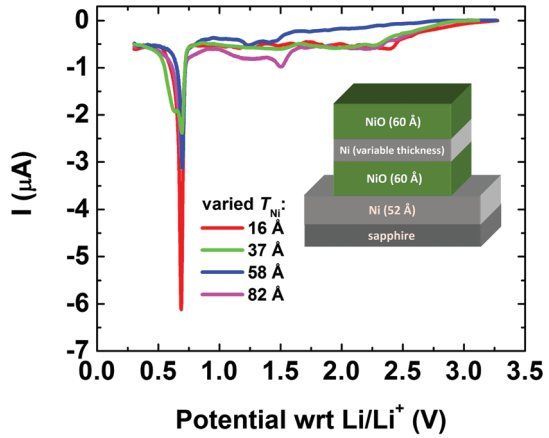

Fig. 7 The first discharge voltammograms of 2-bilayer Ni/NiO electrodes with varied thickness of the Ni layer under the top NiO layer.

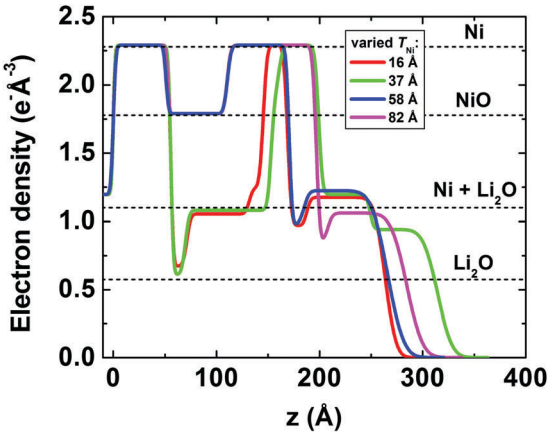

Fig. 8 Electron density profiles for lithiated 2-bilayer Ni/NiO films with varied thickness of the Ni layer in the top bilayer obtained from best fits of XRR data shown in Fig. S4 (ESI†).

the corresponding electron density profiles for pristine films in Fig. S3, ESI†). The first discharge voltammograms and XRR measurements of these 2-bilayer films were performed similarly to trilayer film studies. Fig. 7 shows the first discharge scans for these films. The characteristic abrupt lithiation for all 2-bilayer films was observed at 0.69–0.70 V that is similar value for 5-bilayer films. We conclude that the lithiation voltage is mainly determined by the top NiO layer in multilayer films with different numbers of bilayers. The amount of inserted lithium estimated from these voltammograms shows that the structures with 16 Å and 37 Å thick Ni layers (under the top NiO layer) are fully lithiated, whereas the films with 58 Å and 82 Å show only 50% of theoretical capacity for the two NiO layers in these films. This suggests that only one of the two NiO layers is lithiated. It should be noted that the voltammogram for the 2-bilayer film with Ni layer of 37 Å thick is slightly different from typical voltammogram for NiO films. The reduction peak has asymmetrical shape with major current maximum at 0.69 V, and secondary maximum at 0.63 V corresponding to charge transfer at a lower potential. We propose that this profile indicates a two step lithiation reaction for the 2-bilayer Ni/NiO film. Firstly, the top NiO layer is lithiated, but thickness of underlying Ni layer is, apparently, too thick for lithium ions to penetrate through the Ni layer at that potential. The penetration of the lithium ions to the second NiO layer is then reflected by the appearance of an additional minimum in the first discharge scan.

XRR patterns and the corresponding electron density profiles for the 2-bilayer Ni/NiO films with varied thickness of the Ni layer in the top bilayer after the first discharge are presented in Fig. S4 (ESI†) and Fig. 8, correspondingly. Electron density profiles confirm the voltammetry based conclusion about complete lithiation of 2-bilayer films with Ni layer thicknesses of 16 Å and 37 Å. As can be seen from Fig. 8, the NiO electron densities for these films are near the value that was calculated for a fully lithiated NiO film that retains a stoichiometric ratio between Ni and Li_2O. For the structures with thicker Ni layers (58 Å or 82 Å), XRR analysis shows that lithium ions do not penetrate through these thick layers and only the top NiO layer is lithiated. This result is comparable with the partial lithiation of the 5-bilayer films with 55 Å thick Ni layers (Fig. 2). Our study reveals that the threshold for lithium passage through the Ni buffer layer in a 2-bilayer Ni/NiO film is within the range of 37–58 Å (probably closer to the low limit of this range). This is below the value obtained for multilayer films with a top Ni layer. Similar to the case of the trilayers, XRR analysis (Fig. 8) shows some vertical non-uniformity of the electron density in the lithiated NiO layers; namely the presence of ~15 Å-thick low density regions at each Ni/NiO + Li_2O interface for the lithiated films. The observed deviations of the electron density of the lithiated outer layer of NiO from the calculated value of 1.10 e^- $Å^{-3}$ for a lithiated NiO film consisting of a stoichiometric composition of Ni and Li_2O can be explained by the presence of a Li_2O-rich layer. Consistent with this interpretation is the observation by XRR that Ni film thickness increased by 6–7 Å for all Ni interlayers of the fully lithiated film (or 3–4 Å if only the top NiO layer is lithiated). This reveals that the increase in the Ni buffer layer thickness is adjacent to the low-density layers found within the lithiated NiO layer.

Further insights into the vertical and lateral spatial variation of the structure and composition of the lithiated NiO layers is obtained with a fully lithiated 2-bilayer Ni/NiO sample having a 16 Å thick top Ni layer that was analyzed using STEM imaging and spectroscopy techniques. High angle annular dark field (HAADF) STEM imaging was used to reveal the layer ordering of the structure and to provide qualitative composition information, as the primary contrast mechanism in HAADF STEM images occurs from differential electron scattering due to changes in the average atomic number of each layer. As seen in Fig. 9A, HAADF STEM imaging reveals each layer in the structure, with the brightest layers consisting of Ni, which have the highest average atomic number. This image confirms the general results found by XRR data (see Fig. 8), namely the two-fold expansion of each oxide layer during lithiation. Precise EELS line scans were carried out to confirm the composition of each layer of the cross-section. Close attention was given to the oxygen K edge signal from the

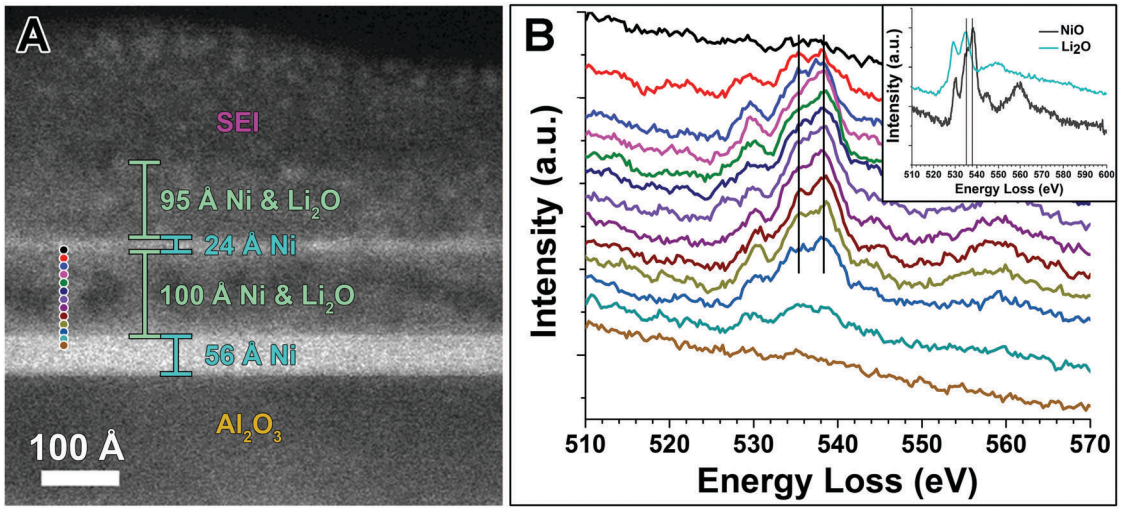

Fig. 9 EELS analysis of 2-bilayer Ni/NiO cross-section sample. (A) HAADF STEM image of lithiated film with colored markers indicating collection areas of EELS spectra in B. (B) Oxygen K EELS linescan results (color coded and offset vertically top to bottom, as the regions of interest in (A)), with lines specifying features of interest in the fine structure at 535 eV and 538 eV. Inset shows oxygen K EELS spectra of NiO and Li_2O standard samples.

lower layer of NiO that underwent conversion to Ni and Li_2O, as seen in Fig. 9B, in order to determine changes in composition throughout the thickness of the individual layer. The oxygen K edge fine structure has distinct features at 535 eV and 538 eV, which can be used to identify and differentiate between Li_2O and NiO, respectively (Fig. 9B, inset). Spectra collected progressively further down in the layer show increasing prominence of the oxygen K edge feature at 535 eV, suggesting an increasing concentration of Li_2O at the bottom of the layer.

A multiple linear least squares (MLLS) fitting procedure was used to analyze the EELS data from Fig. 9. This MLLS fitting is typically used for extracting weak edge signals from the EELS background, isolating signals from overlapping edges in both low-loss and core-loss EELS regions, or mapping elemental compositions.[29–31] The MLLS procedure involves fitting a spectrum with an expression of the form

$$F(E) = AE^{-r} + \sum_n B_n S_n(E), \quad (1)$$

where the first term is represents the background preceding the edge of interest with a typical power-law function, and the second term represents the summation of the input reference spectra $S_n(E)$ multiplied by the calculated fitting coefficients B_n,[32] and is readily applied using the built-in function found in the Gatan Digital Micrograph software. This MLLS fitting differentiates between oxygen in the different electronic environments of NiO and Li_2O.

The core-loss reference spectra shown in the inset of Fig. 9B were used as the input reference spectra for MLLS fitting of the 13 line scan spectra found in Fig. 9. Fig. 10A shows a MLLS fit of the oxygen K edge spectrum 8 (indicated in the inset), which used a fitting range of 532 eV to 550 eV in order to encompass only the primary oxygen K edge features. This MLLS fit is representative of the kind of fits found for all other line scan spectra. The coefficient values, B_n from eqn (1), for Li_2O and NiO contributions are plotted in Fig. 10B for each of the 13 spectra shown in Fig. 9, with spectrum 1 indicating the first spectrum of the line scan (black line) and spectrum 13 indicating the final spectrum of the line scan (mustard line), at the top and bottom of the lithiated NiO layer, respectively. Most notably, the coefficient value of Li_2O begins to increase dramatically in spectra 10 through 13, signaling an increase in contribution of the Li_2O reference spectra to the MLLS fit. This suggests an increase in Li_2O concentration close to the interface with the bottom Ni layer. This result is consistent with the X-ray reflectivity data that showed areas of lower electron density close to the interface with the bottom Ni layer (Fig. 8). Additionally, the coefficient values indicate a variable Li_2O composition throughout the converted Ni and Li_2O structure. These results accurately reflect the oxygen K fine structure evolution seen in Fig. 9. The presence of the feature at 538 eV, which corresponds to NiO, is unexpected in this region of the sample as it should have been reduced during conversion, but can be attributed to oxidation of the Ni reaction product when exposed to air while handling the sample during preparation and loading into the TEM (for details see ESI,† Fig. S5 and S6 and accompanying text).

To check if the non-uniformity at the active/buffer layer interfaces for a lithiated 2-bilayer film is intrinsic to the electrochemistry of conversion reaction rather than the *ex situ* conditions of the X-ray experiment, we performed *in operando* XRR measurements of the structural changes in 2-bilayer films during the first discharge of a half-cell consisting of the film and a lithium metal reference electrode under potentiostatic control starting at the open circuit conditions. XRR scans were repeatedly recorded during the cycle while the potential was swept at a rate of 0.1 mV s^{-1}. Partial lithiation was observed for a 2-bilayer film with nominal 40 Å and 65 Å thick Ni buffer layers and ~50 Å thick active NiO layers. Fig. S7 (ESI†) and Fig. 11 show the sequence of XRR patterns and the corresponding electron density profiles for this film during lithiation.

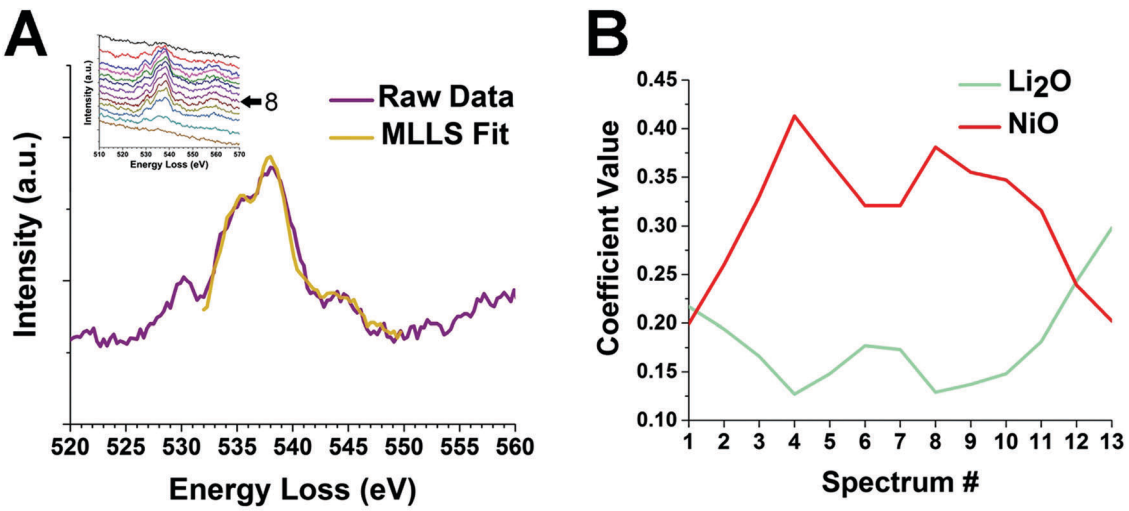

Fig. 10 MLLS fitting of oxygen K EELS edge. (A) Representative example of MLLS fit to oxygen K EELS edge from Fig. 9B spectrum 8. The inset shows the entire EELS line scan data set from Fig. 9B. (B) Plot of MLLS coefficient values for the Li_2O and NiO contribution to the oxygen K edge fine structure for the line scan spectra from Fig. 9B.

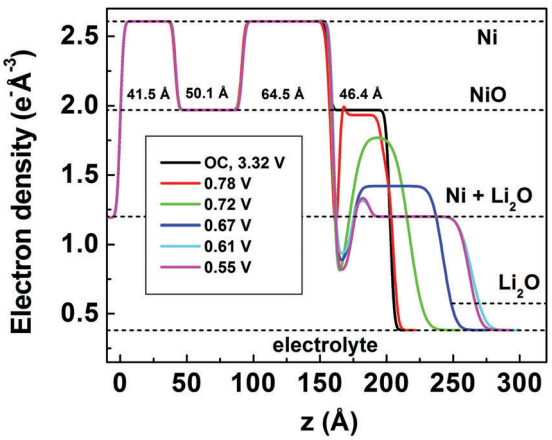

Fig. 11 Electron density profiles obtained from best fits of the XRR data shown in Fig. S7 (ESI†).

It is interesting to see from Fig. 11, that lithium insertion and the related conversion reaction starts at a potential (0.78 V) that is slightly higher than the potential that is normally seen for this electrode (0.71 V). This initial lithiation process of the top NiO layer starts at the Ni/NiO interface (the interfacial nucleation precedes the 3D (random) nucleation of the nickel in the oxide layer[13]) and at the surface of the NiO film (in the ~10 Å range). Fig. S8 (ESI†) shows results of *in operando* XRR data for a 2-bilayer Ni/NiO film with a rather thin top Ni layer (12.6 Å). Both active layers are fully lithiated with the expected expansion of their thicknesses. A low-density region is formed at the Ni/Ni + Li_2O interface in the first bilayer near substrate, but the top lithiated active layer is rather uniform.

Generally, our *ex situ* and *in operando* XRR results lead to the following conclusions: (i) only the top NiO layer is lithiated if the underlying Ni buffer layer is too thick (>65 Å), (ii) a 14 Å low-density region is formed at the Ni/lithiated NiO interface as result of the conversion reaction, with a density that corresponds to that of Li_2O, (iii) the thickness of the Ni layers increases by 3–4 Å (for partial lithiation) or 6–7 Å (for fully lithiated 2-bilayer film). Except for the behaviour at the Ni–NiO interface the electron density of lithiated active layers drops to a value nearly equivalent to the calculated value of 1.20 e^- $Å^{-3}$, corresponding to the stoichiometric composition of Ni and Li_2O associated with fully lithiated NiO layers. The density changes are accompanied by two-fold expansion of the active layers. Density modulations near the film interfaces can be explained by the ultrathin topology of the film structure (the thickness of the top NiO in pristine film is 46.4 Å) that promotes some localization of the reduced Ni close to that interface. Some differences in the electron density profiles of the top active layers for fully lithiated 2-bilayer films observed from *ex situ* and *in operando* XRR data can be explained by different experimental conditions during the XRR experiment.

Evaluation of lithium transport limitations through Ni layers

Transport of lithium ions through a multilayer film structure is associated with the microscopic diffusion and migration of ions under the influence of gradients in Li concentration and chemical potential. The effective lithium ion migration energy barrier is determined by the statistical average of all possible migration pathways and is strongly related to the structure of the solid electrode material, including the type and/or thickness of the top layer in the Ni/NiO bilayer electrode. Comparison of lithiation for trilayer and 2-bilayer electrodes leads us to conclude that lithium ions can pass through a Ni/NiO bilayer if its effective Ni thickness (*i.e.*, the equivalent film thickness based only on the amount of deposited Ni) is less than ~75 Å. Consequently, a bilayer structure with a 60 Å thick NiO film (equivalent to 35 Å of Ni) can be expected to show lithiation for Ni buffer layers that are less than 40 Å-thick (*i.e.*, 75–35 Å). This is close to the experimentally observed value (37 Å). This

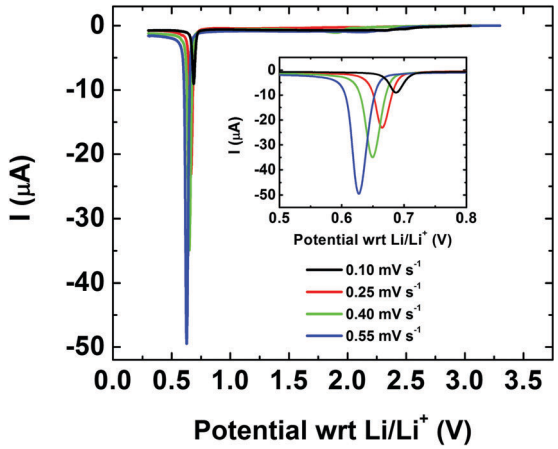

Fig. 12 Scan rate-dependent first discharge voltammograms of 2-bilayer Ni/NiO electrodes in the range of 0.1 to 0.55 mV s^{-1}. Voltammograms in the region of the reduction peak potential are shown in the inset.

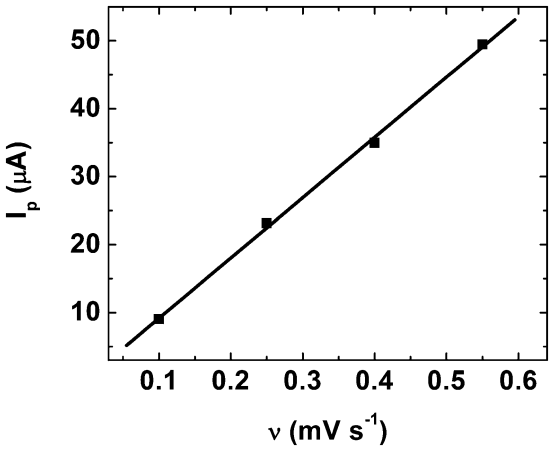

Fig. 13 Scan rate-dependence of the peak current for 2-bilayer Ni/NiO electrodes.

additional barrier for ionic transport through active layers might be dependent on the structure of the top Ni/Li_2O lithiated layers as well, since the lithiation process of multilayer Ni/NiO electrodes starts at the top layers and then progresses vertically toward the bottom of the stack.[16]

What is the mechanism for charge transfer in multilayer electrodes? We used cyclic voltammetry to probe the variation in the reduction feature shape as a function of scan rate to clarify the kinetics of lithium ion insertion in 2-bilayer Ni/NiO electrodes.[33] A set of identical 2-bilayer films (Fig. S9, ESI†) was prepared for this experiment. Fig. 12 shows the voltammetry curves measured for four of these 2-bilayer electrodes at potential scan rates from 0.1 to 0.55 mV s^{-1} during the first discharge. The peak voltage and current of the reduction peak changes as a function of potential scan rate. Estimated capacity for all scan rates varies in the range 8–9 $\times$ 10^{-4} mA h, which is very similar to that estimated from the composition and size of the film – 7.5 $\times$ 10^{-4} mA h. The FWHM of the reduction peak is approximately the same for all scan rates: 0.026–0.028 V. The dependence of the peak current (I_p) on the potential scan rate (ν) can be used to determine the rate limiting step associated with lithium ion diffusion.[33–37] The scan rate dependence of the peak current for 2-bilayer electrodes (Fig. 13) reveals that the peak current changes linearly as a function of scan rate.

It is known that when the peak current is proportional to the potential scan rates (rather than the square root of the scan rate), the process of Li^+ insertion is determined by charge transfer at the liquid/solid interface (rather than by diffusion). This process is described by the equation:[33]

$$I_p = \frac{n^2F^2A\Gamma\nu}{4RT} = S\nu, \quad (2)$$

where the number of electrons transferred in the redox event is n = 2, T is the temperature (293 K here), R – the gas constant (8.314 J K^{-1} mol^{-1}), F – the Faraday constant (96 485 C mol^{-1}) and $A\Gamma$ is the number of moles of active material in the film (1.25 $\times$ 10^{-8} mol). The experimentally obtained slope value (from Fig. 13) is S = 0.089 $\pm$ 0.002 C V^{-1}, which is close to the value $S \sim 0.05$ C V^{-1} predicted in eqn (2) by Bard and Faulkner. Our results, therefore indicate that the conversion reaction is not intrinsically diffusion limited at the level of these few nm-thick films, but that Li^+ insertion into the 2-bilayer Ni/NiO electrodes over this range of scan rates follows ideal thin-layer behavior under surface reaction control.

Conclusions

New insights were obtained into the topological controls over the lithiation of model Li-ion battery electrode structures, comprised of Ni/NiO bilayers with active NiO layers sandwiched between buffer Ni layers and grown on sapphire *via* pulsed laser deposition. The morphological changes accompanying lithiation were tracked *via in situ* and *ex situ* X-ray reflectivity and cross-sectional transmission electron microscopy. (1) Lithiation of the NiO layers were observed by XRR and TEM to change the thickness and density of the lithiated NiO layers indicating conversion into Ni + Li_2O. (2) Complete lithiation of multilayer Ni/NiO films with active NiO layers sandwiched between buffer Ni layers occurs only when the effective Ni thickness of the Ni/NiO bilayers (*i.e.*, the sum of the Ni thickness plus 0.59 times the NiO thickness) is less than $\sim$75 Å, a thickness corresponding to a effective barrier threshold for lithium ion diffusion through Ni. For bilayer thicknesses larger than the threshold value, partial lithiation of the multilayer electrodes is observed – in which only the top NiO layer is lithiated. (3) Lithiation of NiO layers in a multilayer stack leads to significant changes at the Ni–NiO interface including a 3–4 Å increase in the thickness of the adjacent Ni layer and the formation of a low density Li_2O layer corresponding to an idealized conversion reaction with full separation of the reaction products, consistent with our previous findings.[16] (4) Finally, the kinetics of Li^+ insertion into multilayer Ni/NiO thin film electrodes during the first discharge at low scan rates is determined to be controlled by the charge transfer at the liquid/solid interface.

Our results point to the importance of a vertically digitized architecture for controlling the transport of lithium ions and the role interfaces and spatial confinement for a rational design of high-performance Li-ion battery multilayer electrodes. Since transport properties additionally change with the degree of lithiation and cycling history, morphological evolution of multilayer thin film electrodes during lithiation becomes complicated and requires further theoretical and experimental research.

Acknowledgements

This research was supported by the Center for Electrochemical Energy Science, an Energy Frontier Research Center funded by the US Department of Energy, Office of Science, Office of Basic Energy Sciences, under Contract No. DE-AC02-06CH11357. We thank the beamline staff at 33BM and DND-CAT, Advanced Photon Source (APS), which provided valuable assistance. DND-CAT is supported by E. I. duPont de Nemours & Co., Northwestern University, Dow Chemical Co., the State of Illinois through the Department of Commerce and the Board of Education (HECA), and the US National Science Foundation. The samples were grown at the Pulsed Laser Deposition Facility of the Materials Research Center at Northwestern University supported by the National Science Foundation's MRSEC program (DMR-1121262). We acknowledge the use of Northwestern facilities including the NUANCE Center and X-ray Diffraction Facility also supported by MRSEC.

References

1 S. Goriparti, E. Miele, F. D. Angelis, E. D. Fabrizio, R. P. Zaccaria and C. Capiglia, Review on recent progress of nanostructured anode materials for Li-ion batteries, *J. Power Sources*, 2014, **257**, 421–443.

2 J. B. Kim, H. Y. Lee, K. S. Lee, S. H. Lim and S. M. Lee, Fe/Si multi-layer thin film anodes for lithium rechargeable thin film batteries, *Electrochem. Commun.*, 2003, **5**(7), 544–548.

3 J. B. Kim, B. S. Jun and S. M. Lee, Improvement of capacity and cyclability of Fe/Si multilayer thin film anodes for lithium rechargeable batteries, *Electrochim. Acta*, 2005, **50**(16-17), 3390–3394.

4 H. X. Li, H. M. Bai, Z. L. Tao and J. Chen, Si-Y multi-layer thin films as anode materials of high-capacity lithium-ion batteries, *J. Power Sources*, 2012, **217**, 102–107.

5 H. K. Kang, S. R. Lee, W. I. Cho and B. W. Cho, Effect of multilayer structure on cyclic performance of Si/Fe anode electrode in lithium-ion secondary batteries, *Phys. Chem. Chem. Phys.*, 2013, **15**(5), 1569–1577.

6 J. Wang, Y. F. Tong, Z. Xu, W. H. Li, P. X. Yan and Y. W. Chung, Amorphous silicon/carbon multilayer thin films as the anode for high rate rechargeable Li-ion batteries, *Mater. Lett.*, 2013, **97**, 37–39.

7 T. T. Fister, J. Esbenshade, X. Chen, B. R. Long, B. Shi, C. M. Schleputz, A. A. Gewirth, M. J. Bedzyk and P. Fenter, Lithium intercalation behavior in multilayer silicon electrodes, *Adv. Energy Mater.*, 2014, **4**(7), 1301494(6).

8 Y. F. Tong, Z. Xu, C. Liu, G. A. Zhang, J. Wang and Z. G. Wu, Magnetic sputtered amorphous Si/C multilayer thin films as anode materials for lithium ion batteries, *J. Power Sources*, 2014, **247**, 78–83.

9 C. L. Pang, N. Li and C. X. Wang, Intercalated SiO_2&Si/carbon composite for high capacity Li ion battery anodes, *Electrochim. Acta*, 2014, **141**, 226–233.

10 M. T. Demirkan, L. Trahey and T. Karabacak, Cycling performance of density modulated multilayer silicon thin film anodes in Li-ion batteries, *J. Power Sources*, 2015, **273**, 52–61.

11 T. Mori, C. J. Chen, T. F. Hung, S. G. Mohamed, Y. Q. Lin, H. Z. Lin, J. C. Sung, S. F. Hu and R. S. Liu, High specific capacity retention of graphene/silicon nanosized sandwich structure fabricated by continuous electron beam evaporation as anode for lithium-ion batteries, *Electrochim. Acta*, 2015, **165**, 166–172.

12 M. Ashuri, Q. R. He and L. L. Shaw, Silicon as a potential anode material for Li-ion batteries: where size, geometry and structure matter, *Nanoscale*, 2016, **8**(1), 74–103.

13 P. Poizot, S. Laruelle, S. Grugeon, L. Dupont and J. M. Tarascon, Nano-sized transition-metaloxides as negative-electrode materials for lithium-ion batteries, *Nature*, 2000, **407**(6803), 496–499.

14 A. Mukhopadhyay and B. W. Sheldon, Deformation and stress in electrode materials for Li-ion batteries, *Prog. Mater. Sci.*, 2014, **63**, 58–116.

15 J. Cabana, L. Monconduit, D. Larcher and M. R. Palacín, Beyond intercalation-based Li-ion Batteries: the State of the Art and Challenges of Electrode Materials Reacting through conversion reactions, *Adv. Mater.*, 2010, **22**(35), E170–E192.

16 G. Evmenenko, T. T. Fister, D. B. Buchholz, Q. Li, K.-S. Chen, J. Wu, V. P. Dravid, M. C. Hersam, P. Fenter and M. J. Bedzyk, Morphological evolution of multilayer Ni/NiO thin film electrodes during lithiation, *ACS Appl. Mater. Interfaces*, 2016, **8**(31), 19979–19986.

17 X. Sun, W. Si, X. Liu, J. Deng, L. Xi, L. Liu, C. Yan and O. G. Schmidt, Multifunctional Ni/NiO hybrid nanomembranes as anode materials for high-rate Li-ion batteries, *Nano Energy*, 2014, **9**, 168–175.

18 W. Sun, X. Rui, J. Zhu, L. Yu, Y. Zhang, Z. Xu, S. Madhavi and Q. Yan, Ulrtathin nickel oxide nanosheets for enhanced sodium and lithium storage, *J. Power Sources*, 2015, **274**, 755–761.

19 M. Park, X. C. Zhang, M. D. Chung, G. B. Less and A. M. Sastry, A review of conduction phenomena in Li-ion batteries, *J. Power Sources*, 2010, **195**(24), 7904–7929.

20 G. A. Tritsaris, K. Zhao, O. U. Okeke and E. Kaxiras, Diffusion of lithium in bulk amorphous silicon: a theoretical study, *J. Phys. Chem. C*, 2012, **116**, 22212–22216.

21 T. T. Fister, B. R. Long, A. A. Gewirth, B. Shi, L. Assoufid, S. S. Lee and P. Fenter, Real-time observations of interfacial lithiation in a metal silicide thin film, *J. Phys. Chem.*, 2012, **116**, 22341–22345.

22 E. Karapetrova, G. Ice, J. Tischler, H. W. Hong and P. Zschack, Design and performance of the 33-BM beamline

at the Advanced Photon Source, *Nucl. Instrum. Methods Phys. Res., Sect. A*, 2011, **649**(1), 52–54.

23 A. Nelson, Co-refinement of multiple-contrast neutron/X-ray reflectivity data using MOTOFIT, *J. Appl. Crystallogr.*, 2006, **39**, 273–276.

24 L. Cao, D. X. Wang and R. Wang, NiO thin films grown directly on Cu foils by pulsed laser deposition as anode materials for lithium ion batteries, *Mater. Lett.*, 2014, **132**, 357–360.

25 X. L. Sun, C. L. Yan, Y. Chen, W. P. Si, J. W. Deng, S. Oswald, L. F. Liu and O. G. Schmidt, Three-dimensionally "curved" NiO nanomembranes as ultrahigh rate capability anodes for Li- ion batteries with long cycle lifetimes, *Adv. Energy Mater.*, 2014, **4**(4), 1300912(6).

26 Y. Q. Zhu, H. Z. Guo, Y. Wu, C. B. Cao, S. Tao and Z. Y. Wu, Surface-enabled superior lithium storage of high-quality ultrathin NiO nanosheets, *J. Mater. Chem. A*, 2014, **2**(21), 7904–7911.

27 K. Tasaki, A. Goldberg, J.-J. Lian, M. Walker, A. Timmons and S. J. Harris, Solubility of lithium salts formed on the lithium-ion battery negative electrode surface in organic solvents, *J. Electrochem. Soc.*, 2009, **156**(12), A1019–1027.

28 F. Lin, D. Nordlund, T. C. Weng, Y. Zhu, C. M. Ban, R. M. Richards and H. L. Xin, Phase evolution for conversion reaction electrodes in lithium-ion batteries, *Nat. Commun.*, 2014, **5**, 3358(9).

29 R. D. Leapman and C. R. Swyt, Separation of overlapping core edges in electron energy loss spectra by multiple-least-squares fitting, *Ultramicroscopy*, 1988, **26**(4), 393–403.

30 H. Shuman and A. P. Somlyo, Electron energy loss analysis of near-trace-element concentrations of calcium, *Ultramicroscopy*, 1987, **21**(1), 23–32.

31 S. Estradé, L. Yedra, A. López-Ortega, M. Estrader, G. Salazar-Alvarez, M. D. Baró, J. Nogués and F. Peiró, Distinguishing the core from the shell in MnO_x/MnO_y and FeO_x/MnO_x core/shell nanoparticles through quantitative electron energy loss spectroscopy (EELS) analysis, *Micron*, 2012, **43**(1), 30–36.

32 R. F. Egerton, *Electron Energy-Loss Spectroscopy in the Electron Microscope*, Springer US, Boston, MA, 3rd edn, 2011.

33 J. A. Bard and L. R. Faulkner, *Electrochemical Methods: Fundamentals and Applications*, John Wiley & Sons, New York, 2nd edn, 2001.

34 N. Ding, J. Xu, Y. X. Yao, G. Wegner, X. Fang, C. H. Chen and I. Lieberwirth, Determination of the diffusion coefficient of lithium ions in nano-Si, *Solid State Ionics*, 2009, **180**, 222–225.

35 J. P. Zheng, D. J. Crain and D. Roy, Kinetic aspects of li intercalation in mechano-chemically processed cathode materials for lithium ion batteries: electrochemical characterization of ball-milled $LiMn_2O_4$, *Solid State Ionics*, 2011, **196**, 48–58.

36 H. Li, H. Bai, Z. Tao and J. Chen, Si-Y multi-layer thin films as anode materials of high-capacity lithium-ion batteries, *J. Power Sources*, 2012, **217**, 102–107.

37 M. Opitz, J. Yue, J. Wallauer, B. Smarsly and B. Roling, Mechanisms of charge storage in nanoparticulate TiO_2 and $Li_4Ti_5O_{12}$ anodes: new insights from scan rate-dependent cyclic voltammetry, *Electrochim. Acta*, 2015, **168**, 125–132.